Catalysis Science & Technology

ROYAL SOCIETY OF CHEMISTRY

PAPER

View Article Online
View Journal

Cite this: DOI: 10.1039/d6cy00510a

Theoretical insights into designing β-M@Ni(OH)$_2$ electrocatalysts for efficient urea oxidation

Jingwen Zhou and Leanne D. Chen *

Ni-based catalysts show great potential for the urea oxidation reaction (UOR) due to their high activity, low cost, and broad energy and environmental applications. Herein, we investigate two possible mechanisms for N_2 formation on β-Ni(OH)$_2$ using density functional theory (DFT) and further focus on the dehydrogenation steps of the intramolecular pathway over β-Ni(OH)$_2$ and β-M@Ni(OH)$_2$ catalysts (M = Cr, Fe, Co, Cu, Mo, Ru, Rh, Pd, Ir, Pt, and Au). The results show that the intramolecular pathway is energetically favourable on β-Ni(OH)$_2$, and that the enhanced urea adsorption energy, E_{ads}(urea), over β-M@Ni(OH)$_2$ is closely associated with the upshift of the d-band centre, ε_d, induced by M-doping. Gibbs free energy analyses identify β-Fe@Ni(OH)$_2$, β-Co@Ni(OH)$_2$, and β-Pd@Ni(OH)$_2$ as promising catalysts with low limiting potentials. Furthermore, the urea adsorption strength shows a linear correlation with the calculated limiting potentials, suggesting that it can serve as an effective descriptor for urea oxidation toward N_2 formation. This study provides theoretical guidance for the screening and design of highly active Ni-based UOR catalysts.

Received 19th April 2026,
Accepted 21st May 2026

DOI: 10.1039/d6cy00510a

rsc.li/catalysis

1. Introduction

The electrochemical urea oxidation reaction (UOR) is regarded as a cost-efficient and environmentally sustainable strategy in terms of environmental protection and energy storage and conversion.[1–3] For example, the UOR shows great potential in urea-rich wastewater treatment as well as in direct urea fuel cells.[4,5] Moreover, as an anodic reaction, the UOR represents an attractive alternative to the oxygen evolution reaction (OER) in hydrogen generation due to its substantially lower theoretical potential (1.23 V and 0.066 V *vs.* RHE for the OER and UOR, respectively).[6] However, the UOR involves complicated six proton-coupled electron transfer steps in the reaction, which limits its efficiency and overall performance.[2,7] Therefore, effective electrocatalysts are usually required to reduce the overpotential and accelerate the reaction kinetics.[3,8–10]

The exploration of UOR catalysts in recent years has increasingly focused on Ni-based materials, including bimetallic (*e.g.*, NiFe,[11–14] NiCo,[15–18] NiCu,[19,20] NiPt,[21,22] NiPd,[23,24] and NiRh[25–27]) and trimetallic systems (*e.g.*, Ni–Pt–Ir,[28] PtPdNi/C,[29] and $Mn_{0.5}Ni_{2.0}Fe_{0.5}$/rGO[30]) due to their remarkable catalytic performance and long-term durability.[31] Moreover, the surface of Ni-based catalysts can be gradually oxidized to higher-valence Ni species, such as NiO, Ni(OH)$_2$, and NiOOH, under alkaline conditions.[10] These reconstructed Ni-based surfaces, particularly Ni(OH)$_2$-derived structures, are widely considered as the active sites for the UOR.[7,31,32] To further enhance catalytic activity, doping Ni with a secondary metal has emerged as an effective strategy. For example, Wang *et al.* experimentally and computationally investigated the effect of Co doping on the AOR performance of Ni(OH)$_2$.[33] The optimized 5% Co–Ni(OH)$_2$ exhibited the highest catalytic activity (1.357 V *vs.* RHE at 100 mA cm^{-2}) and excellent stability (over 100 h at 10 mA cm^{-2}). This improvement was attributed to the Co dopant, which modulated the electronic structure of Ni(OH)$_2$ *via* an inductive effect, leading to a reduced Ni^{2+}/Ni^{3+} redox potential and facilitating the formation of active NiOOH species. These experimental observations were further supported by DFT calculations, showing that the d-band centre of Co-NiOOH is upshifted relative to NiOOH, which strengthens the adsorption of reaction intermediates and promotes the reaction. Pd incorporation has also been shown to enhance catalyst stability by reducing the strong adsorption of CO_2 on Ni(OH)$_2$. For example, Mathew *et al.* employed a facile two-step room-temperature method to synthesize Pd/Ni(OH)$_2$ catalysts.[34] Electrochemical analysis revealed maximum current densities of 180 mA cm^{-2} and 380 mA cm^{-2} for Ni(OH)$_2$ and Pd/Ni(OH)$_2$, respectively.

Although introducing a second transition metal into Ni-based catalysts has led to noticeable improvements in UOR performance, extensive experimental studies have demonstrated that multiple factors, including the reaction environment,[35–37] catalyst surface structure,[38,39] and electronic structure modulation induced by metal doping,[40] can significantly influence N_2 selectivity and activity, leading

Electrochemical Technology Centre, Department of Chemistry, University of Guelph, Guelph, Ontario N1G 2W1, Canada. E-mail: leanne.chen@uoguelph.ca

to increased complexity in reaction mechanisms and pathway selection. Therefore, further theoretical studies should clarify key mechanistic aspects, including the identification of active sites, the role of key intermediates in governing reaction activity, and the pathways responsible for N–N coupling. In addition, current studies mainly focus on doping 3d transition metals,[14,16,20,41–44] while the development of effective descriptors in theoretical works is crucial for the large-scale screening and evaluation of high-performance Ni-based catalysts. In this work, β-$Ni(OH)_2$ was selected as the parent structure for the UOR because it provides a well-defined structure for systematically investigating the UOR process.[45] Compared with other oxidized Ni-based surfaces, which may involve more complex surface environments and variable O/OH surface states under electrochemical conditions.[46] M@$Ni(OH)_2$ was constructed by doping representative 3d, 4d, and 5d transition metals onto the $Ni(OH)_2$ surface, where M = Cr, Fe, Co, Cu, Mo, Ru, Rh, Pd, Ir, Pt, and Au, to examine and compare their UOR performance and reaction mechanisms.

2. Computational methods

2.1. Structures

We adopted the optimized bulk β-$Ni(OH)_2$ (mp-27 912) structure from our group's previous work,[47] which was selected from the Materials Project and is consistent with experimental results. A (2 × 2 × 4) β-$Ni(OH)_2$ slab model was constructed, in which the top two layers were fully relaxed, the bottom two layers were fixed, and a 16 Å vacuum region was introduced along the z direction between adjacent images. In addition, a surface Ni atom was substituted by an M atom to generate β-M@$Ni(OH)_2$ (M = Cr, Fe, Co, Cu, Mo, Ru, Rh, Pd, Ir, Pt, and Au), with a surface dopant concentration of 25%.

2.2. Calculation settings

All calculations were performed using spin-polarized periodic density functional theory (DFT) as implemented in the Vienna *ab initio* Simulation Package (VASP),[48,49] in combination with the Atomic Simulation Environment (ASE) interface.[50] The projector augmented-wave (PAW) pseudopotentials[51,52] were used to describe the core–valence interactions with an energy cutoff of 500 eV. van der Waals interactions between the adsorbates and alloy surfaces were accounted for using the DFT-D3 dispersion correction.[53] Moreover, a 4 × 4 × 1 (8 × 8 × 1) Monkhorst–Pack k-point mesh[54] was used for geometry optimization (density of states calculations). Geometry optimizations were performed until the total energy and atomic forces converged to below 10^{-5} eV and 0.05 eV A^{-1}, respectively. The generalized gradient approximation with a Hubbard U correction (GGA + U) was applied to selected metals, and the values are listed in Table 1.[47,55] The Gibbs free energies (ΔG) of the elementary steps involved in the UOR were calculated using a previously reported CHE model:[56]

Table 1 Hubbard U parameters for different metal atoms

Metal	Hubbard U (eV)
Ni	5.50
Cr	2.25
Fe	4.00
Co	3.72
Cu	6.75
Ir	2.00

$$\Delta G = \Delta E + \Delta E_{ZPE} + \int_0^T \Delta C_p dT - T\Delta S - eU \quad (1)$$

where ΔE is the reaction energy obtained from DFT calculations, $\int_0^T \Delta C_p dT$ accounts for the thermal contribution to enthalpy, T denotes the absolute temperature, U represents the applied electrode potential, e is the elementary charge, and ΔS denotes the entropy change. The effect of pH = 14 was also considered in this work to be consistent with experimental conditions.[57] Adsorption free energies were referenced to a clean surface and urea(g), H_2(g), as well as H_2O(l). The equilibrium potentials (U_{eq}) for N_2 formation *via* intramolecular and intermolecular mechanisms were taken as U_{eq} = −0.76 V *versus* RHE and U_{eq} = −0.55 V *versus* RHE, respectively.[58] Moreover, the definition of the d-band centre (ε_d) is obtained as the average energy of the entire d-band:[59]

$$\varepsilon_d = \frac{\int_{-\infty}^{\infty} \varepsilon\, \rho(\varepsilon) d\varepsilon}{\int_{-\infty}^{\infty} \rho(\varepsilon) d\varepsilon} \quad (2)$$

where ε and $\rho(\varepsilon)$ refer to the energy of the orbital states and the density of states (DOS) at energy ε, respectively.[60] ε_d values for all calculations were extracted from the calculated results using the analysis tool VASPKIT.[61]

3. Results and discussion

3.1. Mechanism on pristine $Ni(OH)_2$

The generally accepted mechanisms for N_2 formation in the UOR on Ni-based catalysts can be classified into two categories, intramolecular and intermolecular,[4] as shown in Fig. 1. In the intramolecular mechanism, one turnover of the reaction involves only one urea molecule.[62] Specifically, urea undergoes successive dehydrogenation to form the *CON_2 intermediate, accompanied by intramolecular N–N coupling. The subsequent cleavage of the C–N bond in *CON_2 generates N_2(g) and *CO, with *CO being further oxidized to CO_2. In the intermolecular mechanism, N–N coupling involves nitrogen species derived from two different urea molecules.[58] Urea undergoes dehydrogenation to form the *$CO(NH)_2$ intermediate, followed by C–N bond cleavage to generate NCO^- (aq) and *NH species. The resulting *NH then couples with another *NH and is further dehydrogenated to N_2.

We first calculated the free energy diagrams for urea oxidation to N_2 formation based on two

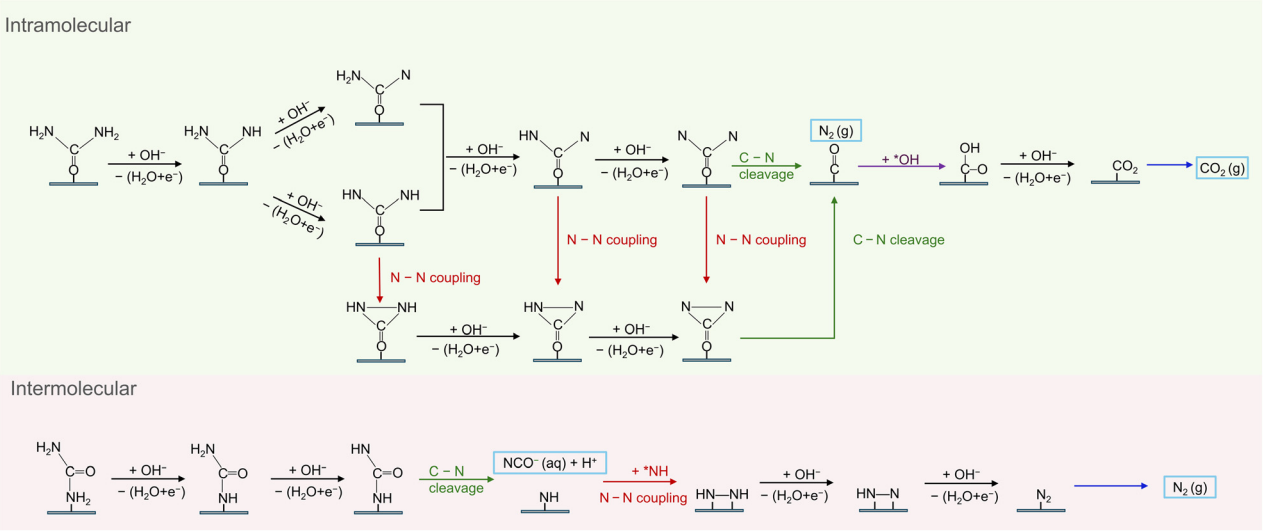

Fig. 1 Representative mechanisms for N_2 formation in the UOR.

mechanisms. For the intramolecular mechanism, the initial adsorption configuration of urea involves the binding of the O atom to surface Ni atoms at a hollow site, and the adsorption energy E_{ads}(urea) is −0.84 eV. In addition, during the first four dehydrogenation steps of the intramolecular mechanism, the second dehydrogenation step, namely the asymmetric deprotonation from *OCNHNH$_2$ to *OCNNH$_2$, requires a lower free energy than the symmetric formation of *OCNHNH, due to the stronger adsorption of *OCNNH$_2$ (Fig. 2(a)). The corresponding energy difference is 0.29 eV. The further deprotonation of *OCNNH$_2$ is identified as the potential-determining step (PDS) in the intramolecular mechanism, with a free energy of 1.31 eV. Notably, the N–N bond gradually forms during this step, with the bond length decreasing from 2.373 Å in *OCNNH$_2$ to 1.733 Å in *OCNNH. All remaining steps after the first four dehydrogenation steps are exergonic except for CO_2 desorption. The limiting potential (U_{lim}) of the intramolecular pathway is 0.55 V. Accordingly, reducing the free energy of *OCNNH$_2$ deprotonation is the key to enhancing the overall reaction activity on β-Ni(OH)$_2$ in the intramolecular mechanism.

For the intermolecular mechanism, the N atom of urea points toward the surface. The configuration after the first dehydrogenation step, *NHCONH$_2$, is distinct from the intramolecular case, where the N atom serves as the adsorption site and favours subsequent intermolecular N–N coupling.[4] This adsorption energy of urea is −0.52 eV. The free energy diagram indicates that the symmetric dehydrogenation of *NHCONH$_2$ to *NHCONH is the PDS along the intermolecular pathway, and the corresponding free energy is 1.34 eV, as shown in Fig. 2(b). In addition, the subsequent C–N bond cleavage of *NHCONH is thermodynamically unfavourable. This step remains energetically uphill even at the limiting potential (U_{lim} = 0.79 V for the intermolecular pathway), because it is a non-electrochemical step. Comparing the free energy profiles of the two mechanisms, the PDS for both pathways are located within the first four dehydrogenation steps, and the intramolecular mechanism for urea oxidation toward N_2 is energetically preferred over the intermolecular mechanism. These results are in agreement with previous studies that also identified early-stage dehydrogenation as the energetically critical process and the intramolecular pathway as the preferred mechanism for the UOR on Ni-based hydroxide catalysts.[34,40,58,63] Therefore, in this work, we employed calculations of the first four steps in the intramolecular mechanism as an efficient strategy to screen high-performance UOR β-M@Ni(OH)$_2$ catalysts.

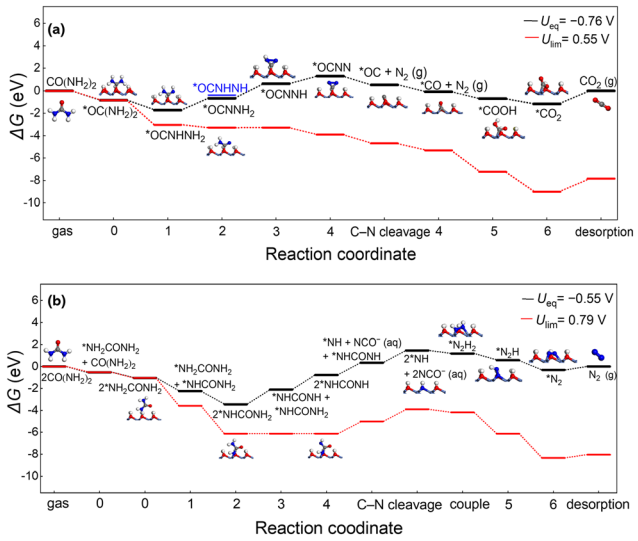

Fig. 2 Gibbs energy diagrams for the intramolecular (a) and intermolecular (b) pathways over pristine β-Ni(OH)$_2$.

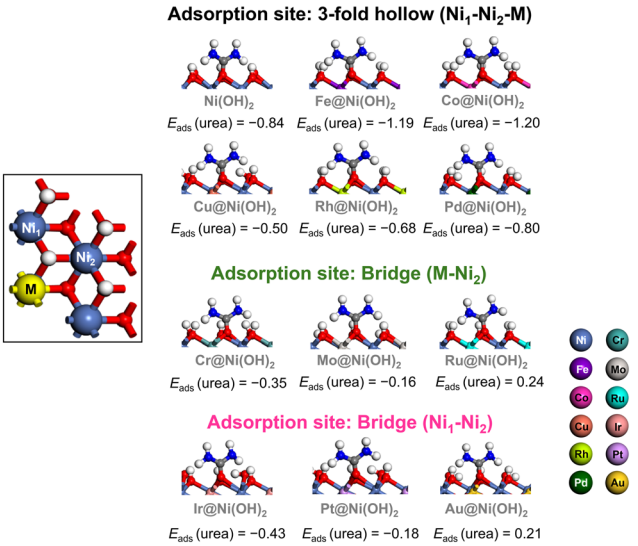

Fig. 3 Optimized urea adsorption configurations and adsorption energies E_{ads}(urea) in eV over the β-Ni(OH)$_2$ and β-M@Ni(OH)$_2$ surfaces. The inset shows the various adsorption sites.

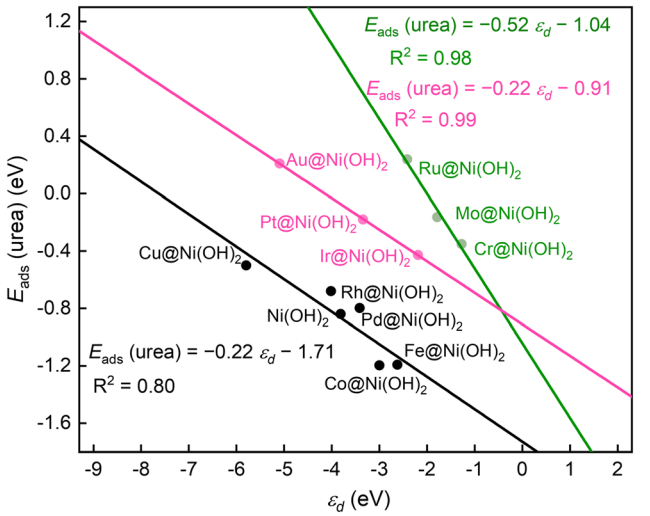

Fig. 4 Correlation between the adsorption energy of urea, E_{ads}(urea), and the d-band centre, ε_d, grouped by the most favoured adsorption site on pristine β-Ni(OH)$_2$ and β-M@Ni(OH)$_2$.

3.2. D-band Centre analysis

The adsorption configurations of urea on β-Ni(OH)$_2$ and β-M@Ni(OH)$_2$ are classified into three groups according to the adsorption sites, as shown in Fig. 3. The configurations of Fe@Ni(OH)$_2$, Co@Ni(OH)$_2$, Cu@Ni(OH)$_2$, Rh@Ni(OH)$_2$, and Pd@Ni(OH)$_2$ are consistent with that on pristine Ni(OH)$_2$, where the O atom preferentially occupies a threefold hollow site (Ni$_1$–Ni$_2$–M). The remaining configurations adopt bridge-site geometries with different coordinating atoms, for example, configurations of Cr@Ni(OH)$_2$, Mo@Ni(OH)$_2$, and Ru@Ni(OH)$_2$ adsorb at the M–Ni$_2$ bridge site, whereas configurations of Ir@Ni(OH)$_2$, Pt@Ni(OH)$_2$, and Au@Ni(OH)$_2$ occupy the bridge site formed by two Ni atoms, the Ni$_1$–Ni$_2$ site. The bond lengths between the oxygen atom of urea and the surface metal atoms (Ni or M) are summarized in Table 2. The calculated E_{ads}(urea) values indicate that adsorption at the bridge sites is generally weaker than at the threefold hollow site.

We further calculated the d-band centre (ε_d) of β-Ni(OH)$_2$ and β-M@Ni(OH)$_2$, where the surface atoms were selected according to the most favourable urea adsorption sites. Linear relationships between the ε_d and E_{ads}(urea) were observed for each adsorption-site group, as shown in Fig. 4. These results suggest that the variation in urea adsorption strength upon M-doping correlates with the shift of the d-band centre toward the Fermi level, suggesting that an upshift of the d-band centre generally favors stronger urea adsorption. Although adsorption configurations and local structural effects may also contribute to the adsorption behavior, the modulation of the d-band centre still provides a useful electronic explanation for understanding the observed adsorption trends within the present systems.

3.3. Comparison of pristine Ni(OH)$_2$ and M@Ni(OH)$_2$

Fig. 5 systematically compares the dehydrogenation pathways on β-Ni(OH)$_2$ and β-M@Ni(OH)$_2$. The order of

Table 2 Adsorption site, O–metal (Ni/M) bond lengths of adsorbed urea in Å, and bond length differences |Δ*l*| on β-Ni(OH)$_2$ and β-M@Ni(OH)$_2$

Dopant	Adsorption site	O–Ni$_1$	O–Ni$_2$	O–M	|Δ*l*|
Pristine	Ni$_1$–Ni$_2$–M	2.36	2.25	2.26	0.11
Fe	Ni$_1$–Ni$_2$–M	2.32	2.20	2.31	0.12
Co	Ni$_1$–Ni$_2$–M	2.32	2.21	2.26	0.11
Cu	Ni$_1$–Ni$_2$–M	2.26	2.20	2.31	0.11
Rh	Ni$_1$–Ni$_2$–M	2.41	2.24	2.34	0.17
Pd	Ni$_1$–Ni$_2$–M	2.29	2.18	2.31	0.13
Cr	M–Ni$_2$	2.52	2.16	2.15	0.37
Mo	M–Ni$_2$	2.50	2.20	2.19	0.31
Ru	M–Ni$_2$	2.58	2.15	2.14	0.44
Ir	Ni$_1$–Ni$_2$	2.13	2.22	2.72	0.59
Pt	Ni$_1$–Ni$_2$	2.30	2.22	2.61	0.39
Au	Ni$_1$–Ni$_2$	2.16	2.21	2.69	0.53

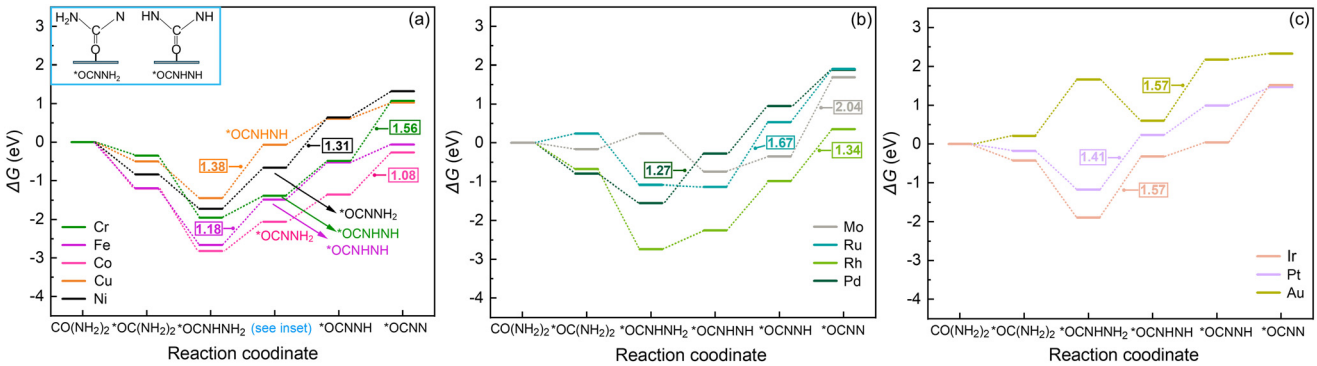

Fig. 5 Gibbs energy diagrams for the dehydrogenation steps of the intramolecular pathway on β-Ni(OH)$_2$ and β-M@Ni(OH)$_2$ catalysts doped with (a) 3d, (b) 4d, and (c) 5d M transition metals (M = Cr, Fe, Co, Cu, Mo, Ru, Rh, Pd, Ir, Pt, and Au). The number inside the rectangle represents the free energy of the potential-determining step for each catalyst.

dehydrogenation steps on these M-doped catalysts is divided into two different classes. For example, Co@β-Ni(OH)$_2$, similar to pristine β-Ni(OH)$_2$, favours asymmetric dehydrogenation from *OCNHNH$_2$ to form *OCNNH$_2$, whereas the remaining β-M@Ni(OH)$_2$ surfaces prefer symmetric dehydrogenation from *OCNHNH$_2$ to generate *OCNHNH. In addition, doping with M atoms can alter the PDS and its free energy on specific β-M@Ni(OH)$_2$ surfaces. Based on their PDS, the surfaces were divided into three groups. (1) When the PDS is the second dehydrogenation step, *i.e.*, dehydrogenation of *OCNHNH$_2$, the surfaces are β-Fe@Ni(OH)$_2$, β-Cu@Ni(OH)$_2$, β-Pd@Ni(OH)$_2$, β-Ir@Ni(OH)$_2$, and β-Pt@Ni(OH)$_2$. (2) When the PDS is the third dehydrogenation step, it corresponds to the dehydrogenation of *OCNNH$_2$ on pristine β-Ni(OH)$_2$, whereas for β-Ru@Ni(OH)$_2$ and β-Au@Ni(OH)$_2$ it corresponds to the dehydrogenation of *OCNHNH. (3) Lastly, when PDS is the last dehydrogenation step, *i.e.*, the dehydrogenation of *OCNNH, the surfaces are β-Cr@Ni(OH)$_2$, β-Co@Ni(OH)$_2$, β-Mo@Ni(OH)$_2$, and β-Rh@Ni(OH)$_2$. The free energies of these PDSs follow the order of 1.08 eV < 1.18 eV < 1.27 eV < 1.31 eV < 1.34 eV < 1.38 eV < 1.41 eV < 1.56 eV < 1.57 eV ≈ 1.57 eV < 1.67 eV < 2.04 eV on the β-Co@Ni(OH)$_2$, β-Fe@Ni(OH)$_2$, β-Pd@Ni(OH)$_2$, β-Ni(OH)$_2$, β-Rh@Ni(OH)$_2$, β-Cu@Ni(OH)$_2$, β-Pt@Ni(OH)$_2$, β-Cr@Ni(OH)$_2$, β-Ir@Ni(OH)$_2$, β-Au@Ni(OH)$_2$, β-Ru@Ni(OH)$_2$, and β-Mo@Ni(OH)$_2$ surfaces, respectively. These calculated free energies show that β-Co@Ni(OH)$_2$, β-Fe@Ni(OH)$_2$, and β-Pd@Ni(OH)$_2$ are promising high-performance UOR catalyst candidates, and the results are in agreement with previous experimental studies,[33,34,40,63] suggesting that doping Co, Fe, and Pd on β-Ni(OH)$_2$ is an effective strategy to enhance the activity of Ni-based catalysts. The calculated U_{lim} for each catalyst is shown in Table 3. The configurations of the first four dehydrogenation steps on β-Ni(OH)$_2$ and β-M@Ni(OH)$_2$ are denoted in Fig. S1. The N–N bond length decreases toward bond formation during the dehydrogenation from *OCNNH$_2$ (or *OCNHNH) to *OCNN, except for β-Mo@Ni(OH)$_2$, β-Ru@Ni(OH)$_2$, β-Rh@Ni(OH)$_2$, and β-Ir@Ni(OH)$_2$. It is worth noting that *OCNN binds to the β-Mo@Ni(OH)$_2$ surface *via* the N atom rather than the O atom, unlike the adsorption configuration on other catalyst surfaces. We will discuss the outlying behaviour of β-Mo@Ni(OH)$_2$ in the following section.

Table 3 Limiting potentials (U_{lim}) of the PDS for the UOR over β-Ni(OH)$_2$ and β-M@Ni(OH)$_2$

Catalyst	U_{lim} (V)
Ni(OH)$_2$	0.55
Cr@Ni(OH)$_2$	0.80
Fe@Ni(OH)$_2$	0.42
Co@Ni(OH)$_2$	0.32
Cu@Ni(OH)$_2$	0.62
Mo@Ni(OH)$_2$	1.28
Ru@Ni(OH)$_2$	0.91
Rh@Ni(OH)$_2$	0.58
Pd@Ni(OH)$_2$	0.51
Ir@Ni(OH)$_2$	0.81
Pt@Ni(OH)$_2$	0.65
Au@Ni(OH)$_2$	0.81

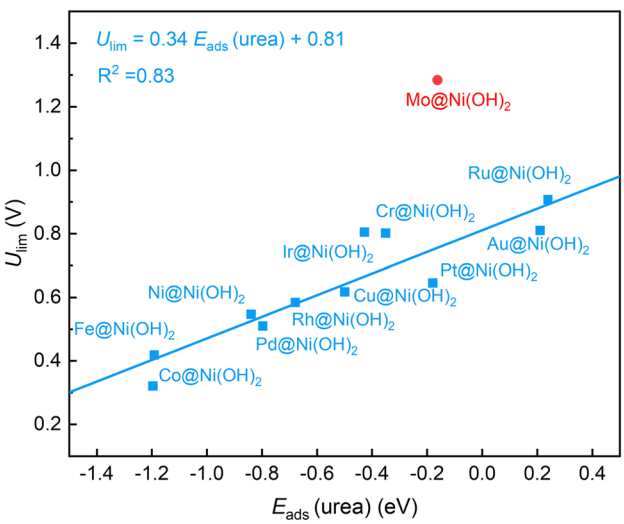

Fig. 6 Linear correlations of E_{ads}(urea) and U_{lim} on Ni(OH)$_2$ and M@Ni(OH)$_2$.

3.4. E_{ads}(urea) as activity descriptor

The establishment of effective descriptors is generally regarded as an efficient bridge linking key adsorbates with catalytic activity, thereby enabling the efficient screening and prediction of high-performance electrocatalysts.[64–66] Here, we observe a linear relationship between E_{ads}(urea) and U_{lim}, *i.e.*, stronger urea adsorption leads to a lower U_{lim} on β-Ni(OH)$_2$ and β-M@Ni(OH)$_2$ (Fig. 6), indicating that high-performance Ni-based UOR catalysts can be achieved by tuning the E_{ads}(urea). A similar trend is also observed on the β-NiOOH surface.[46] It should be noted that excessively strong E_{ads}(urea) may over-stabilize surface intermediates, which may increase the free energy required for subsequent dehydrogenation steps. In practical catalyst design, the balance between adsorption strength and subsequent reaction activity should be further considered, although a detailed investigation of this aspect is beyond the scope of this work.

Notably, β-Mo@Ni(OH)$_2$ still follows the overall trend between E_{ads}(urea) and U_{lim}. However, it appears as an outlier from the linear scaling relationship. This deviation originates from the adsorption configuration in the potential-determining step. On the other β-M@Ni(OH)$_2$ catalyst surfaces, the *OCNN intermediate generally maintains a stable O–bound adsorption configuration. However, on β-Mo@Ni(OH)$_2$, the high oxophilicity of the Mo dopant leads to an overly strong Mo–O interaction during geometry optimization. This strong interaction competes with the intrinsic O–C bonding within the *OCNN intermediate, leading to cleavage of the O–C bond and destabilization of the original intermediate structure. In contrast, when adopting an N-bound adsorption configuration, such as *NCON on β-Mo@Ni(OH)$_2$, the intermediate structure can remain intact because the direct strong interaction between O and Mo is avoided (see Fig. S1 in the SI). However, the rearrangement of the adsorption structure from an O-bound to an N-bound configuration on β-Mo@Ni(OH)$_2$ considerably increases the free energy of the potential-determining step. In addition, combined with the relationship between ε_d and E_{ads}(urea) discussed above, we find that the improved catalytic performance induced by M-atom doping can be rationalized by the modulation of ε_d. Therefore, the E_{ads}(urea) serves as an effective descriptor for screening and predicting potential UOR electrocatalysts. We propose that catalysts with adsorption energies of urea around or below −0.84 eV, which is the value on β-Ni(OH)$_2$, including β-Co@Ni(OH)$_2$, β-Fe@Ni(OH)$_2$, and β-Pd@Ni(OH)$_2$, can be promising Ni-based catalysts.

4. Conclusion

In this work, we conducted a systematic investigation of the UOR mechanism and catalytic performance on β-Ni(OH)$_2$ and β-M@Ni(OH)$_2$ surfaces, where M = Cr, Fe, Co, Cu, Mo, Ru, Rh, Pd, Ir, Pt, and Au. The main conclusions are summarized in the following.

1. The free energy diagrams show that the intramolecular pathway is energetically more favourable than the intermolecular pathway on all β-Ni(OH)$_2$ surfaces. Moreover, the dehydrogenation steps in both mechanisms are identified as the PDSs, specifically the dehydrogenation of *OCNNH$_2$ in the intramolecular pathway and the dehydrogenation of *NHCONH$_2$ in the intermolecular pathway.

2. The modulation of the d-band centre induced by M-atom doping plays an important role in the changes in urea adsorption energies on β-Ni(OH)$_2$ and β-M@Ni(OH)$_2$ surfaces.

3. The calculated free energy diagram for the four dehydrogenation steps shows that M-doping can effectively lower the free energy of the PDS and thus the limiting potential. Based on our results, we propose that β-Co@Ni(OH)$_2$, β-Fe@Ni(OH)$_2$, and β-Pd@Ni(OH)$_2$ are promising Ni-based UOR catalyst candidates.

4. The adsorption energy of urea is an effective descriptor for AOR activity. An upshift of the d-band centre generally strengthens the adsorption of urea, which contributes to a reduction in the limiting potential and thus improves catalytic activity. Catalysts with E_{ads}(urea) around or below −0.84 eV, the value on β-Ni(OH)$_2$, can be considered improved Ni-based catalysts for the UOR.

Author contributions

J. Zhou: conceptualization, data curation, formal analysis, validation, visualization, writing original draft, review, and editing. L. D. Chen: conceptualization, funding acquisition, project administration, resources, supervision, writing, review, and editing.

Conflicts of interest

There are no conflicts to declare.

Data availability

The data supporting this article have been included as part of the supplementary information (SI).

Supplementary information: which contains the coordinates for all structures considered in this study. See DOI: https://doi.org/10.1039/d6cy00510a.

Acknowledgements

The authors gratefully acknowledge the Natural Sciences and Engineering Research Council of Canada (Discovery Grant, RGPIN-2020-07095) for financial support of this work. All DFT calculations are enabled by Advanced Research Computing resources generously provided by the Digital Research Alliance of Canada (RRG-5307).

References

1 A. K. Satheesan, R. Madhu, S. Nagappan, H. N. Dhandapani, A. De, S. S. Roy, P. Mazumder and S. Kundu, *Chem. Commun.*, 2025, **61**, 4092–4109.

2 J. Gautam, S.-Y. Lee and S.-J. Park, *Adv. Energy Mater.*, 2025, **15**, 2406047.
3 J. Wang, M. Sun, X. Zhang, J. Liu, J. He, W. Ge, S. Kong, G. Zhang, M. Gao and Z. Sun, *et al.*, *Adv. Mater.*, 2025, e15043.
4 X. Gao, S. Zhang, P. Wang, M. Jaroniec, Y. Zheng and S.-Z. Qiao, *Chem. Soc. Rev.*, 2024, **53**, 1552–1591.
5 G. Gnana kumar, A. Farithkhan and A. Manthiram, *Adv. Energy Sustainability Res.*, 2020, **1**, 2000015.
6 J. J. Medvedev, N. H. Delva and A. Klinkova, *ChemPlusChem*, 2024, **89**, e202300739.
7 Y. Zeng, S. Xiang, S. Lu and X. Qi, *Materials*, 2024, **17**, 2617.
8 S. Xu, X. Ruan, M. Ganesan, J. Wu, S. K. Ravi and X. Cui, *Adv. Funct. Mater.*, 2024, **34**, 2313309.
9 A. S. Rasal, H. M. Chen and W.-Y. Yu, *Nano Energy*, 2024, **121**, 109183.
10 F. Guo, D. Cheng, Q. Chen, H. Liu, Z. Wu, N. Han, B.-J. Ni and Z. Chen, *Prog. Nat. Sci.: Mater. Int.*, 2024, **34**, 362–375.
11 A. Modak, R. Mohan, K. Rajavelu, R. Cahan, T. Bendikov and A. Schechter, *ACS Appl. Mater. Interfaces*, 2021, **13**, 8461–8473.
12 S. C. Dhawale, A. V. Munde, B. B. Mulik, R. P. Dighole, S. S. Zade and B. R. Sathe, *Langmuir*, 2024, **40**, 2672–2685.
13 X. Yin, K. Zhu, K. Ye, J. Yan, D. Cao, D. Zhang, J. Yao and G. Wang, *J. Colloid Interface Sci.*, 2024, **654**, 36–45.
14 Y. Diao, Y. Liu, G. Hu, Y. Zhao, Y. Qian, H. Wang, Y. Shi and Z. Li, *Biosens. Bioelectron.*, 2022, **211**, 114380.
15 B. Feng, W. Jiang, R. Deng, J. Lu, P. Tsiakaras and S. Yin, *J. Colloid Interface Sci.*, 2024, **663**, 1019–1027.
16 X. Gao, Y. Wang, W. Li, F. Li, H. Arandiyan, H. Sun and Y. Chen, *Electrochim. Acta*, 2018, **283**, 1277–1283.
17 W. Xu, H. Zhang, G. Li and Z. Wu, *Sci. Rep.*, 2014, **4**, 5863.
18 W. Yan, D. Wang and G. G. Botte, *Electrochim. Acta*, 2012, **61**, 25–30.
19 M. Wala, A. Blacha-Grzechnik, A. Stolarczyk, S. Bajkacz, P. Dydo and W. Simka, *Int. J. Hydrogen Energy*, 2023, **48**, 34229–34243.
20 A. Abutaleb, *Catalysts*, 2019, **9**, 397.
21 D. Kutyła, M. Fukumoto, H. Takahashi, R. Takahashi, K. Skibi'nska and P. Żabiński, *Materials*, 2025, **18**, 5069.
22 J. R. Barbosa, C. H. Paranhos, O. C. Alves, N. R. Checca, J. P. Serna, A. L. Rossi and J. C. M. Silva, *Electrochim. Acta*, 2020, **355**, 136752.
23 A. Rodríguez-Buenrostro, A. Martínez-Lázaro, M. Contreras-Martínez, A. Sharma, G. L. Barcenas, G. Oza, A. Arenillas, J. Ledesma-García and L. Arriaga, *Mater. Renewable Sustainable Energy*, 2024, **13**, 255–264.
24 N. Muthuchamy, S. Jang, J. C. Park, S. Park and K. H. Park, *ACS Sustainable Chem. Eng.*, 2019, **7**, 15526–15536.
25 P. Mirzaei, S. Bastide, A. Dassy, R. Bensimon, J. Bourgon, A. Aghajani, C. Zlotea, D. Muller-Bouvet and C. Cachet-Vivier, *Electrochim. Acta*, 2019, **297**, 715–724.
26 S. Qian, Z. Rao, Y. Liu, J. Yan, B. Fan, Y. Gui and F. Guo, *Electrochim. Acta*, 2020, **330**, 135211.
27 A. T. Miller, B. L. Hassler and G. G. Botte, *J. Appl. Electrochem.*, 2012, **42**, 925–934.
28 K. Hiraide, Y. Liu, K. Akiyoshi, S. Kuwabata and T. Torimoto, *Electrochemical Society Meeting Abstracts prime2024*, 2024, pp. 3827–3827.
29 M. Pérez-Sosa, E. Ramírez-Meneses, A. Manzo-Robledo, J. Mateos-Santiago, M. Hernández-Pérez, V. Garibay-Febles, L. Lartundo-Rojas and G. Zacahua-Tlacuatl, *Int. J. Hydrogen Energy*, 2021, **46**, 21419–21432.
30 P. Basumatary, U. H. Lee, D. Konwar and Y. S. Yoon, *Int. J. Hydrogen Energy*, 2020, **45**, 32770–32779.
31 C. Zhang, S. Chen, L. Guo, Z. Li, C. Yan and C. Lv, *Chin. J. Chem.*, 2024, **42**, 3441–3468.
32 X. Gao, J. Dong, H. Yang, C. Ni, X. He, Z. Li and L. Tian, *J. Alloys Compd.*, 2025, 178477.
33 Y. Wang, Y. Lu, Y. Shi, J. Wang, Y. Zheng, J. Pan, C. Li and J. Cao, *Appl. Surf. Sci.*, 2023, **640**, 158391.
34 N. Mathew, R. Rathod, S. Saha, P. K. Santra, S. K. Pati and M. Eswaramoorthy, *Chem. - Asian J.*, 2025, **20**, e202401188.
35 C. Fan, M. Zhang, Y. Li, Y. Zhang, Y.-Q. Wang, F. Gong and J. Liu, *Nat. Commun.*, 2026, **17**, 1585.
36 W. Jiang, J. Zhang, J. Wu, Z. Zhai, T. Yu, L. Luo and S. Yin, *Adv. Energy Mater.*, 2026, **16**, e03978.
37 W. Jiang, Z. Zhai, X. Zhuo, J. Wu, B. Feng, T. Yu, H. Wen and S. Yin, *Chin. J. Struct. Chem.*, 2025, **44**, 100519.
38 S. W. Tatarchuk, J. J. Medvedev, F. Li, Y. Tobolovskaya and A. Klinkova, *Angew. Chem., Int. Ed.*, 2022, **61**, e202209839.
39 J. Li, J. Li, T. Liu, L. Chen, Y. Li, H. Wang, X. Chen, M. Gong, Z.-P. Liu and X. Yang, *Am. Ethnol.*, 2021, **133**, 26860–26866.
40 L. Chen, W. Jiang, J. Zhang, B. Chu, Z. Zhai, T. Yu, H. He and S. Yin, *ACS Sustainable Chem. Eng.*, 2024, **12**, 10466–10474.
41 Z. Zhao, Y. Zhou, T. Kang, X. Wu, S. Jin, M. Yuan and X. Chang, *Inorg. Chem.*, 2026, **65**, 5465–5477.
42 Z. Ji, S. Zhao, Z. Wang, L. Hao, J. Li, F. Cheng, M. Hussain, W. Su and J. Liu, *J. Power Sources*, 2026, **674**, 239796.
43 C. Xie, C. Zhou, Y. Zhang, B. Zhou, Y. Yao, B. Li, J. Li, J. Bai, M. Long and K. Jiang, *et al.*, *Angew. Chem., Int. Ed.*, 2026, e25119.
44 W. Jiang, X. Zhuo, T. Yu, J. Lu, Z. Zhai, H. Wen and S. Yin, *ACS Sustainable Chem. Eng.*, 2024, **12**, 998–1006.
45 D. S. Hall, D. J. Lockwood, C. Bock and B. R. MacDougall, *Proc. R. Soc. A*, 2015, **471**, 20140792.
46 Q. Jin, M. X. Garcia-Ortiz and L. Árnadóttir, *J. Catal.*, 2025, 116503.
47 S. J. Johnston, R. M. Choueiri, X. Liu, B. J. Laframboise, S. W. Tatarchuk and L. D. Chen, *J. Phys. Chem. C*, 2024, **128**, 5568–5578.
48 G. Kresse and J. Hafner, *Phys. Rev. B*, 1993, **47**, 558.
49 G. Kresse and J. Furthmuller, *Phys. Rev. B*, 1996, **54**, 11169.
50 A. H. Larsen, J. J. Mortensen, J. Blomqvist, I. E. Castelli, R. Christensen, M. Dułak, J. Friis, M. N. Groves, B. Hammer and C. Hargus, *et al.*, *J. Phys.: Condens. Matter*, 2017, **29**, 273002.
51 P. E. Blöchl, *Phys. Rev. B*, 1994, **50**, 17953.
52 G. Kresse and D. Joubert, *Phys. Rev. B*, 1999, **59**, 1758.
53 S. Grimme, J. Antony, S. Ehrlich and H. Krieg, *J. Chem. Phys.*, 2010, **132**, 154104.
54 H. J. Monkhorst and J. D. Pack, *Phys. Rev. B*, 1976, **13**, 5188.

55 J. Liu, J. Xiao, Z. Wang, H. Yuan, Z. Lu, B. Luo, E. Tian and G. I. Waterhouse, *ACS Catal.*, 2021, **11**, 5386–5395.
56 J. K. Nørskov, J. Rossmeisl, A. Logadottir, L. Lindqvist, J. R. Kitchin, T. Bligaard and H. Jonsson, *J. Phys. Chem. B*, 2004, **108**, 17886–17892.
57 R. K. Singh and A. Schechter, *Electrochim. Acta*, 2018, **278**, 405–411.
58 S. W. Tatarchuk, R. M. Choueiri, A. J. MacKay, S. J. Johnston, W. M. Cooper, K. S. Snyder, J. J. Medvedev, A. Klinkova and L. D. Chen, *ChemPhysChem*, 2024, **25**, e202300889.
59 J. K. Nørskov, F. Studt, F. Abild-Pedersen and T. Bligaard, *Fundamental Concepts in Heterogeneous Catalysis*, John Wiley & Sons, 2014.
60 B. J. Laframboise, J. Coveny, J. Zhou and L. D. Chen, *ChemElectroChem*, 2025, **12**, e202500288.
61 V. Wang, N. Xu, J.-C. Liu, G. Tang and W.-T. Geng, *Comput. Phys. Commun.*, 2021, **267**, 108033.
62 W. Chen, L. Xu, X. Zhu, Y.-C. Huang, W. Zhou, D. Wang, Y. Zhou, S. Du, Q. Li and C. Xie, *et al.*, *Angew. Chem., Int. Ed.*, 2021, **60**, 7297–7307.
63 Z. Zheng, D. Wu, L. Chen, S. Chen, H. Wan, G. Chen, N. Zhang, X. Liu and R. Ma, *Appl. Catal., B*, 2024, **340**, 123214.
64 J. Zhou, J. S. Chung and S. G. Kang, *J. Phys. Chem. C*, 2024, **129**, 303–313.
65 R. K. Sharma, H. Minhas and B. Pathak, *J. Phys. Chem. Lett.*, 2026, **17**, 2689–2701.
66 J. Zhou, J. S. Chung and S. G. Kang, *Int. J. Hydrogen Energy*, 2024, **58**, 745–752.

